Entropy-driven Denaturation for Sustainable Regeneration of Protein Waste

Yichong Wang[1,2,4], Junlang Liu[1,4], Michael Peters[2], Ryoma Ishii[2,3], Dianzhuo Wang[1], Sourav Chowdhury[1], Kevin Kit Parker[2,5*], Eugene I. Shakhnovich[1,5*]

Affiliations

[1] Department of Chemistry and Chemical Biology, Harvard University, Cambridge, MA, 02138 USA

[2] Disease Biophysics Group, John A. Paulson School of Engineering and Applied Sciences, Harvard University, Boston, MA, 02134 USA

[3] Medical & Health Informatics Laboratories, NTT Research, Inc., Sunnyvale, CA, 94085 USA

[4] These authors contributed equally: Yichong Wang, Junlang Liu

***Corresponding authors:**

Kevin Kit Parker
Science and Engineering Complex 6.307
150 Western Ave, Boston, MA 02134
Email: kkparker@seas.harvard.edu
Phone: 617-496-1793

Eugene I. Shakhnovich
12 Oxford Street
Cambridge, MA 02138
Email: shakhnovich@chemistry.harvard.edu
Phone: 617-495-4130

Keywords: Indirect Solute Effect, Entropy-driven, Protein Denaturation, Sustainability, Waste Recycling

Abstract (197/200 words)

Electrolytes are essential parts of the environment for all life forms, where proteins, water, and solutes interplay to support vital activities. However, a fundamental understanding of the effect of ionic solutes on proteins remains elusive for more than a century[1–3]. Here we show how some ionic solutes can serve as potent denaturants despite the absence of direct protein-ion interactions. We demonstrate dramatic differences between denaturation potency of different ionic solutes with lithium bromide (LiBr) being the strongest denaturant and sodium bromide (NaBr) being the least potent. Experiments and simulations indicate the presence of certain ions disrupts the structure of water network, thereby induce protein denaturation indirectly via an entropy-driven mechanism. We further introduce a scalable strategy for protein waste revalorization, distinguished by the closed-loop recycling of denaturants, straightforward protein separation, and facile manufacturing, all enabled by the entropy-driven denaturation by LiBr. Through successful isolation and systematic study of indirect solute effects, our findings suggest a unified and generally applicable framework for decoding of the protein-water-solute nexus, where all current studies can be easily incorporated. Besides, our regeneration approach underscores the feasibility of repurposing protein waste into valuable biomaterials in a sustainable way with wide-reaching application potential.

Introduction

The intricate interactions between proteins, water and solutes determine not only protein structure, but also protein folding and function. Initial observations in the 19th century[1,2] yielded the 'Hofmeister Series', evaluating protein solubility in relation to ionic solutes. Property changes of proteins in concentrated ionic solutions[4–6] and protein denaturation induced by lithium salts[3,7] have been reported since the 1940s. More recently, there has been significant progress in understanding the importance of direct interactions between proteins or water and solutes[8–11], the origin of hydrophobicity[12] and related effects on protein folding[13]. However, a unified framework to understand triadic relationship between proteins, water, and solutes, has remained elusive[14].

This knowledge gap limits our ability to control, mass-produce, and utilize sustainable protein-based materials from renewable resources[15,16]. Due to our limited understanding of protein-water-solute interactions, current protein extraction processes heavily rely on non-recyclable organic chemicals (e.g., urea, guanidine hydrochloride), resulting in pollution, increased costs, and difficulties in further processing and manufacturing[17]. As a result, over ten million tons of keratin-rich waste generated annually, typically disposed through incineration or landfilling instead of being repurposed[18,19]. Such waste is unfortunate as keratin materials possess various desirable properties including biodegradability, biocompatibility, mechanical strength, and chemical modifiability, thereby endowing them with promising potential for versatile applications from sustainable textiles to tissue engineering scaffolds[20,21].

A plausible mechanism of indirect solute effects on protein stability is modulation of hydrophobic effect via water hydrogen bond network changes. To test this hypothesis, we selected a simple monovalent ion pair—lithium bromide (LiBr) as the model solute. Among all the monovalent ion pairs, LiBr has the second largest solubility of all common solvents (e.g., water,

69 methanol, ethanol, etc.)[9] and stability in water in contrast to lithium iodide (LiI). Despite the
70 potential promise of LiBr as a versatile protein denaturant[4], the lack of mechanistic understanding
71 of its action as a denaturant has largely limited its further industrial applications. Here, we
72 systematically explored LiBr's effects on protein structure and denaturation through comparison
73 with both lithium chloride (LiCl) and sodium bromide (NaBr). The capability of LiBr as a universal
74 denaturant has been confirmed by testing three proteins spanning different levels of structure
75 complexity. We further confirmed, both experimentally and theoretically, that the indirect solute
76 effects of LiBr can significantly affect protein structure and stability through altering the structure
77 of water network. Finally, we demonstrated that entropic mechanisms of denaturation, which lacks
78 direct interaction between protein and denaturant, is highly advantageous for scalable protein
79 waste regeneration strategy as it enables closed-loop recycling of LiBr, easy separation of proteins
80 and facile manufacturing.

81 **Universal denaturation capacity of LiBr**

82 To systematically investigate solute effects on protein conformation, we selected three proteins
83 representing different levels of structural complexity (Fig. 1a), along with three different ionic
84 solutes including LiBr, LiCl, and NaBr. We found markedly distinct solute effects for different
85 proteins and salts across various concentrations, as evidenced by aggregation of denatured protein
86 during turbidity measurements at 405 nm (Fig. 1b-d). As the smallest protein tested, dihydrofolate
87 reductase (DHFR) shows significant aggregation at 1 M LiBr and 5 M LiCl, but remains soluble
88 at all NaBr concentrations (Fig. 1b). Since both salt-induced precipitation and denaturation can
89 result in protein aggregation, we used Fourier-transform infrared spectroscopy (FTIR) to further
90 distinguish the underlying mechanisms (Fig. 1e-g, Extended Data Fig. 2a-d). Starting from 2 M
91 LiBr, we observed a gradual loss of secondary structure of DHFR such as α-helix (1650-1655 cm^{-}
92 ^{1}) and β-sheet/turns (1660-1690 cm^{-1}), along with an increase in aggregated β-like random
93 structures (1620-1630 cm^{-1}) (Fig. 1e). The secondary structure loss of DHFR in 2 M LiBr was
94 further confirmed by conformational kinetics measurement using quantitative Raman
95 spectroscopy, where less-stable β-sheet disappeared first, followed by α-helix, with obvious
96 accumulation of aggregated random structures (Fig. 1h). Both FTIR (Extended Data Fig. 2a) and
97 tryptophan fluorescence measurement (Extended Data Fig. 2e) confirmed DHFR unfolding
98 starting from ~5 M LiCl. In contrast, DHFR stays well-folded for all concentrations of NaBr
99 (Extended Data Fig. 2b).

100 To elucidate whether solutes can affect conformations of proteins with more complex,
101 hierarchically-ordered structures, we examined fibronectin. This protein, a critical component for
102 cell-extracellular matrix interactions[22] has more recently been explored as a synthetic building
103 material[23–25] because of its unique structure-function relationships. Fibronectin is comprised of

104 two covalently linked extensible arms formed by β-sheet domains that can undergo quaternary
105 structure changes from globular to extended state[26] (Fig. 1a middle). With the increase of protein
106 structural complexity, higher concentrations of LiBr and LiCl (7 M and 8 M, respectively) were
107 required to induce aggregation of fibronectin (Fig. 1c), where secondary structure loss was also
108 confirmed by FTIR spectra (Fig. 1f, Extended Data Fig. 2c-d). Before denaturation, protein
109 conformational changes were observed through dynamic light scattering (DLS) measurements of
110 the hydrodynamic radius R_h (Fig. 1i), where fibronectin transitions from the globular state (R_h ~8
111 nm) to the extended state (R_h ~23 nm) at a lower concentration of LiBr around 2 M. Combining
112 the secondary and tertiary structure loss observed in FTIR and the quaternary structure extension
113 shown via DLS, we can identify sequential changes in protein structure as the concentration of
114 LiBr increases (Extended Data Fig. 2f).

115 We also tested keratin structural transformation in LiBr solution as observed by
116 Feughelman et al.[4]. In contrast to DHFR and fibronectin, keratin possesses hierarchical structure
117 ranging from α-helices at the nanometer scale to protofibrils and filaments at the micrometer scale.
118 A turbidity map generated from 24-hour soaking of wool in salt solutions showed that visible
119 signal can only be observed at high concentrations of LiBr (Fig. 1d). FTIR spectra further indicated
120 complete denaturation of both α-keratin from wool and β-keratin from goose feathers, irrespective
121 of their different native configurations (Fig. 1g). Finally, scanning electron microscope (SEM)
122 images of wool before and after treatment with 8 M LiBr, LiCl, and NaBr also corroborate our
123 turbidity measurement findings (Fig. 1d), where only concentrated LiBr induces denaturation of
124 keratin (Fig. 1j, Extended Data Fig. 2g).

125

126

127 **Indirect solute effects**

128 Thermodynamically, protein conformational change or denaturation is a complex process where
129 entropy and enthalpy contribute to the overall free energy balance. At lower concentrations of
130 denaturants, entropy and enthalpy balance to favor the native state; however, at higher
131 concentrations, they tend towards the unfolded state[27]. To elucidate the thermodynamic
132 mechanisms of protein denaturation by LiBr, we conducted isothermal titration calorimetry (ITC)
133 experiments to measure the enthalpic contribution from direct LiBr solute-protein interactions,
134 with commonly used denaturants urea and guanidine hydrochloride (GdnHCl) as a control.
135 Pronounced heat release has been detected upon injection of urea or GdnHCl into samples
136 containing DHFR and fibronectin (Fig. 2a,b). Enthalpy changes, dependent on protein sizes and
137 exposures of hydrophobic domains (~-7 kCal mol^{-1} for DHFR and ~-14 kCal mol^{-1} for fibronectin),
138 correspond to the formation of 1-2 or 3-4 hydrogen bonds per organic denaturant molecule,
139 respectively. These results are highly consistent with previous studies[28,29], where enthalpy-driven
140 mechanisms of protein denaturation by urea or GdnHCl were established. In contrast, no enthalpy
141 change from direct interaction with proteins was detected when LiBr solution was injected into
142 protein samples under identical protocols, suggesting that solute ions here do not engage in
143 noticeable direct interactions with proteins. Given that LiBr, being a universal and potent
144 denaturant, does not contribute enthalpically to protein free energy in solution, we conclude that
145 LiBr shifts the free energy landscape of proteins towards denatured state by affecting its entropy.

146 **Mechanism of entropy-driven protein denaturation**

147 To further test the hypothesis of entropy-driven denaturation by LiBr, molecular dynamics (MD)
148 simulations were employed to provide experimentally inaccessible atomistic-level insights. First,
149 we confirmed that local water density around ions (Extended Data Fig. 3a,b) in our simulations

agrees well with previous X-ray and neutron diffraction experimental results[30]. The cooperativity of ion hydration[31] was also observed, where local water structures are determined by both ions and their counterions. Molecular water entropy, encompassing both translational and rotational entropy of water molecules, was calculated based on TIP3P[32] water model using Two-Phase Thermodynamic (2PT) method, the combination of which have been validated as the most accurate for replicating experimental entropy values[33]. In both LiBr and LiCl solutions, two distinct populations of water molecules are detectable (Fig. 2c, Extended Data Fig. 3d,e). As suggested by experimental evidence of local effects of Li^+ ions[34] (Extended Data Fig. 3a,b, and c left), the subset characterized by lower average entropy is identified as ion-bound water, whereas the other, possessing higher entropy, is identified as free water that constitutes the hydrogen bonded water network. LiBr solution also demonstrates a higher proportion of ion-bound water compared to LiCl solution (see Fig. 2c, Extended Data Figs. 3d,e). This enhanced capacity of Li^+ ions to sequester water in LiBr could stem from the more effective separation between Li^+ and Br^- ions, attributable to the lower charge density of Br^- ions and the substantial size disparity between Li^+ and Br^- ions. In contrast, the NaBr solution exhibits a single population akin to the intact hydrogen bond network of pure water (Fig. 2c, Extended Data Fig. 3f), which could potentially be explained by the absence of localized high charge density[12,31] (Extended Data Fig. 3c right).

The prominent differences in both water network size and denaturation capability between LiBr, LiCl, NaBr, and pure water, point out to water network entropy as a possible culprit. To further highlight this concept, we established an analytical model of entropy penalty decrease ($\Delta\Delta S$), which drives the overall free energy balance towards the denatured state.

$$\Delta\Delta S = \Delta\Delta S^{\text{translation}} + \Delta\Delta S^{\text{rotation}} + \Delta\Delta S^{\text{vibration}} - 4k_{\text{B}} \ln \phi \quad (1)$$

173 Here, $\Delta\Delta S^{\text{translation}}$, $\Delta\Delta S^{\text{rotation}}$, and $\Delta\Delta S^{\text{vibration}}$ represent the contributions of water
174 molecular entropy and $-4k_{\text{B}}\ln\phi$ denotes the contribution of water network entropy, with ϕ
175 representing the ratio of water network sizes in ionic solutions and pure water (see **Methods** for
176 derivation of Eq(1) and further details).

177 Notably, the numerical estimates of water entropy penalty decrease, calculated using Eq.(1)
178 with values of individual contributions obtained from molecular dynamics simulation (Fig. 2d,f),
179 align well with our experimental observations regarding the order of denaturation capacities of
180 different salts. For example, ~3 M LiBr and ~5 M LiCl show comparable degree of entropy penalty
181 reduction and exhibit similar protein denaturation capacity as shown by FTIR (Fig. 1e and
182 Extended Data Fig. 2a), while 6 M NaBr exhibits lower entropy penalty reduction than 2 M LiBr
183 and thus cannot denature DHFR (Extended Data Fig. 2b). Furthermore, the decrease in network
184 entropy penalty appears to be the predominant factor over that of rotational and translational
185 entropy of individual water molecules. This key factor has been overlooked in several previous
186 studies leading to considerable controversy regarding the effects of solutes on water dynamics and
187 protein unfolding[35,36].

188 Finally, protein free energy landscapes in different LiBr concentrations were constructed
189 using well-tempered metadynamics simulation[37] (See **Methods** for details), where a stable α-helix
190 peptide of 20 amino acids was adopted as a model protein (Fig. 2e). The increase of concentrations
191 shifts the free energy landscapes and lowers the energy barrier for unfolding, which lend further
192 confirmation of the universal denaturation capacity of LiBr. In conclusion, solute-induced water
193 network disruption potentiates the reduction of entropy penalty when proteins sequester water
194 molecules from bulk water network during unfolding, and thus facilitates the unfolding process
195 and leads to large-scale protein conformational changes and denaturation (Fig. 2g).

196 **Sustainable keratin regeneration with facile manufacturing**

197 In contrast with conventionally applied enthalpy-driven denaturants (e.g., urea, GdnHCl), the
198 entropy-driven denaturation mechanism can address limitations in protein regeneration, including
199 the waste and pollution from single-use organic chemicals and the complexity of fabrication.
200 Hereby, we developed an economic and sustainable protocol for keratin-rich waste regeneration
201 with closed-loop recycling of LiBr solution followed by facile manufacturing (Fig. 3a). Protein
202 resources such as animal fragments or wool-based textiles are denatured by an aqueous solution
203 of 8 M LiBr, with heat applied to accelerate reaction kinetics and prevent aggregation during
204 extraction. A small amount of 1,4-dithiothreitol (DTT) is added as a reductant to break down the
205 dense disulfide matrix in keratin. After extraction, the mixture is hot filtered, cooled down and
206 separated into a subnatant of denatured keratin gel and a supernatant of LiBr solution driven by
207 spontaneous aggregation (Extended Data Fig. 4b,c). Since the LiBr does not induce denaturation
208 via direct interactions, the resulting solution can be continuously recycled in a closed loop, which
209 not only eliminates pollution from waste organics but also significantly reduces the consumption
210 and cost of denaturants.

211 To test the cyclic stability of the closed-loop recycling protocol, we performed multiple
212 iterations of extraction using both α-keratin from wool and β-keratin from goose feathers. The
213 yield remains consistently around 40% after five cycles of extraction (Fig. 3b), while the first cycle
214 exhibits a slightly lower yield possibly due to a small amount of keratin remaining in the solution
215 after separation. Unchanged composition of the recycled LiBr solution is further confirmed with
216 thermogravimetric analysis (TGA) and coupled Fourier transform infrared spectroscopy (TG-
217 FTIR) of the emerging gas (Fig. 3c, Extended Data Fig. 4d,e).

218 Notably, in the absence of direct binding to denaturants, the spontaneous aggregation of
219 denatured keratin enables a simple separation of condensed gel from the solution, alleviating
220 difficulties with conventional organic reagents (Fig. 3d), which usually involves dialysis and
221 lyophilization. Additionally, the separated keratin can undergo a fast phase transition from
222 denatured gel state to renatured solid state when transferring back into water (Fig. 3e,
223 Supplementary Video 1), while keratin extracted with organic denaturants remains non-
224 processable until fully dialyzed. The viscous property of the gel and the fast phase transition
225 process enable a wide array of manufacturing modalities including injection molding, film casting,
226 dip coating, fiber spinning, and 3D printing (Fig. 3f) without any additional usage of organic
227 solvents.

228 **Mechanical tunability and shape-memory of regenerated keratin**

229 Keratins, particularly α-keratins, contain multiple cysteine residues, which form a dense network
230 of intermolecular disulfide bonds. After extraction, these disulfide bonds are reduced to thiol
231 groups, thereby endowing the regenerated keratin material with adjustable covalent crosslinking
232 through oxidation. For instance, low level of crosslinking allows the α-helices to rearrange more
233 freely under stress (Fig. 4a, Extended Data Fig. 5a). As a result, reduced keratin preserves a high
234 flexibility with a modulus of 124.3 ± 18.8 kPa and a yield strain of 435 ± 61%. On the contrary,
235 formation of multiple disulfide bonds can significantly increase the elastic modulus of oxidized
236 keratin by an order of magnitude to 1.35 ± 0.11 MPa and decrease the fracture strain to 95 ± 9%
237 (Fig. 4b,e, Extended Data Fig. 5b-e). Raman spectroscopy of keratin samples under 50% strain
238 suggests that most secondary structure remain unchanged within reduced keratin upon stretching,
239 whereas a more discernible loss of α-helix domains and an increase of β/random structures can be
240 observed in oxidized keratin (Fig. 4c). Differences between the two conditions reveal the effect of

241 disulfide crosslinking on the α-helix network of regenerated keratin, providing the material with
242 tunable mechanical properties from ductile to elastic (Fig. 4f).

243 In addition to enhancing the mechanical strength, disulfide crosslinking can also provide
244 the keratin material with a hydration-responsive shape-memory property. Prior studies of Miserez
245 et al.[38] and Cera et al.[39] revealed that uniaxial strain can induce reversible uncoiling of α-helix into
246 metastable β-like structures within anisotropic bio-based elastomer. Similarly, in the crosslinked
247 keratin network, the transition between coiled helix and uncoiled strands was also observed (Fig.
248 4d), leading to a shape-memory effect facilitated by formation and decay of hydrogen bonds. In a
249 hydrated environment, dynamic reformation of hydrogen bonds enables the uncoiling of helices
250 under external stress, allowing the material to be deformed into a temporary shape. Upon
251 dehydration, the formation of intermolecular hydrogen bonds then locks the uncoiled chains,
252 thereby fixing the network in the temporary shape. Finally, upon rehydration, presence of free
253 water molecules can unlock the hydrogen bonds again, facilitating the recovery of native α-helix
254 structures and returning the material to its permanent shape (Fig. 4g). The shape-memory
255 capability of regenerated keratin is demonstrated both as a standalone object and as components
256 of a more complex tensegrity structure (Fig. 4h, Supplementary Video 2-4). Sustainable keratin
257 materials may show promise in a variety of applications, including areas such as smart textiles or
258 biomedical implants, due to their biocompatible nature, tunable mechanical properties, and shape-
259 memory capability.

260

261 # Discussion

262 The effect of water networks on conformations and stability of proteins has been a subject of
263 extensive debate. We investigated the molecular mechanism of the hierarchical protein

conformational change in the presence of three monovalent salts—LiBr, LiCl, and NaBr. Most surprisingly we found no direct interactions between proteins and ionic solutes despite the significant potency of LiBr as a universal denaturant. Thermodynamic and spectroscopic analyses, in combination with atomistics molecular simulations, have shown that large-scale protein conformational changes and denaturation by LiBr and other ionic solutes are mediated by reduction of entropy penalty. Localized strong solute-water interactions for LiBr, and, to a lesser extent, LiCl, disrupt the water network and reduce the entropy penalty that proteins incur when sequestering water molecules from bulk water phase during denaturation. In contrast, water network is largely preserved in NaBr solution, thereby consistently retaining protein native structures across varying concentrations. With the confirmation of entropic effect of ionic solutes on protein-water interactions, our study provides a comprehensive understanding of protein-water-solute nexus, offering potentially valuable insights into the crucial role that water plays in protein folding, functions, and evolution.

Leveraging the distinctive advantages of this entropy-driven mechanism, we have developed a regeneration strategy for protein waste featuring closed-loop recycling of LiBr solution, simple protein separation, and diverse manufacturing pathways. The resulting keratin material demonstrates tunable mechanical properties and hydration triggered shape-memory capability. This interdisciplinary study, where clear illustration of molecular-level mechanism meets scalable novel applications, opens promising avenues for future valorization of mistreated wastes and development of protein-based smart materials, and offers practical strategies for advancing towards a sustainable economy.

Figures

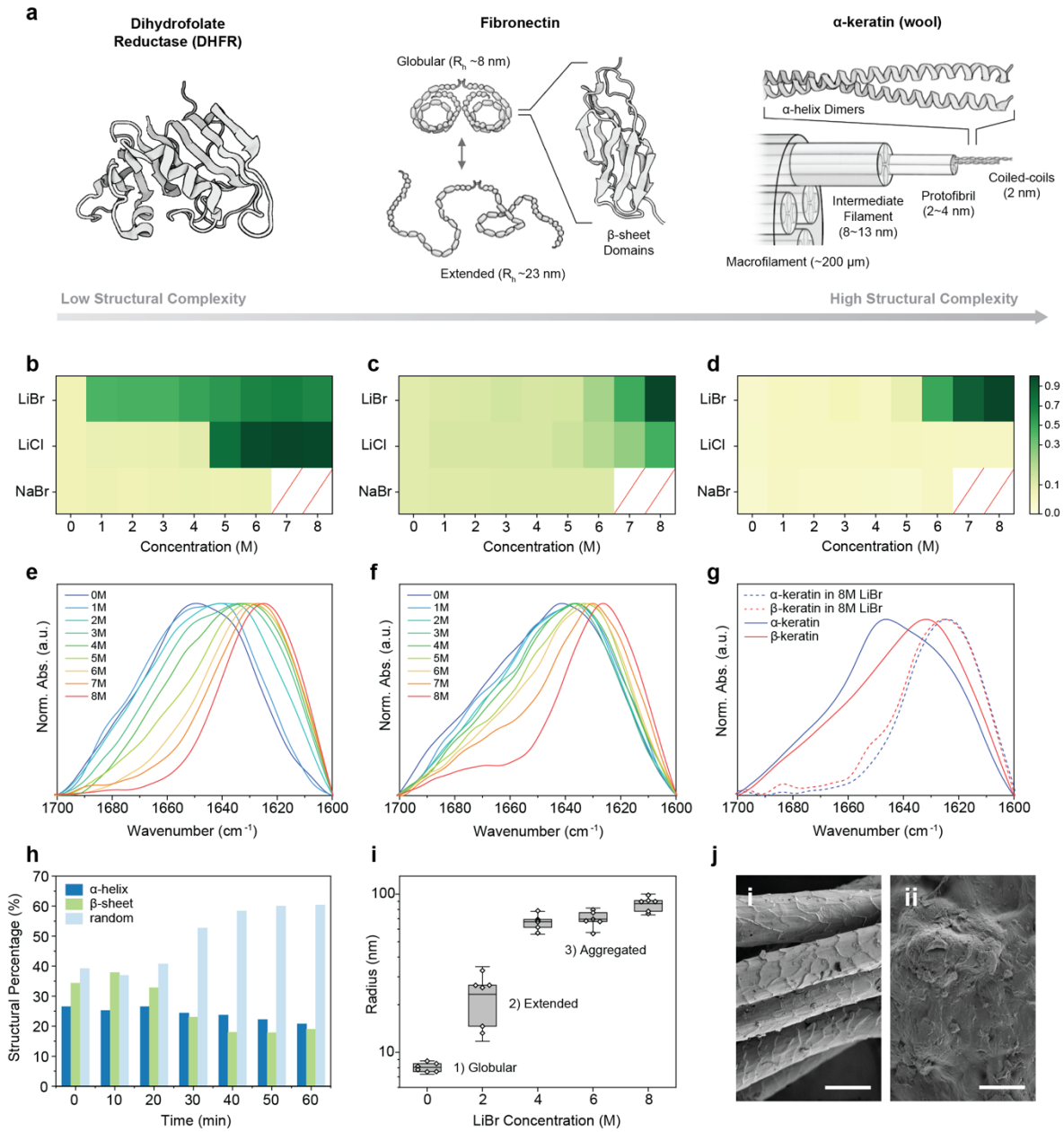

Fig. 1 | Concentrated LiBr solutions induce universal protein conformational change and cause denaturation. a, Schematics of DHFR, fibronectin, and α-keratin (wool), representing three levels of structural complexity. **b-d**, Turbidity assay of three respective proteins measured by OD_{405}, suggesting different denaturation capabilities of LiBr, LiCl, and NaBr. Data are normalized by the highest OD_{405} values of respective proteins and presented as mean (n = 4). **e-g**, FTIR of the amide I band indicate a gradual loss of secondary structure upon increasing of LiBr concentration. **h**, Percentage change of the secondary structure in DHFR in 2 M LiBr, deconvoluted from the amide I band of Raman spectra. **i**, DLS measurement of the hydrodynamic radius of fibronectin with increasing LiBr concentration, indicating an extension of quaternary structure followed by aggregation. Data are presented as mean ± 1.5 s.d. (n = 6). **j**, SEM image of wool prior (i) and after (ii) denaturation with 8 M LiBr. Scale bars, 50 μm.

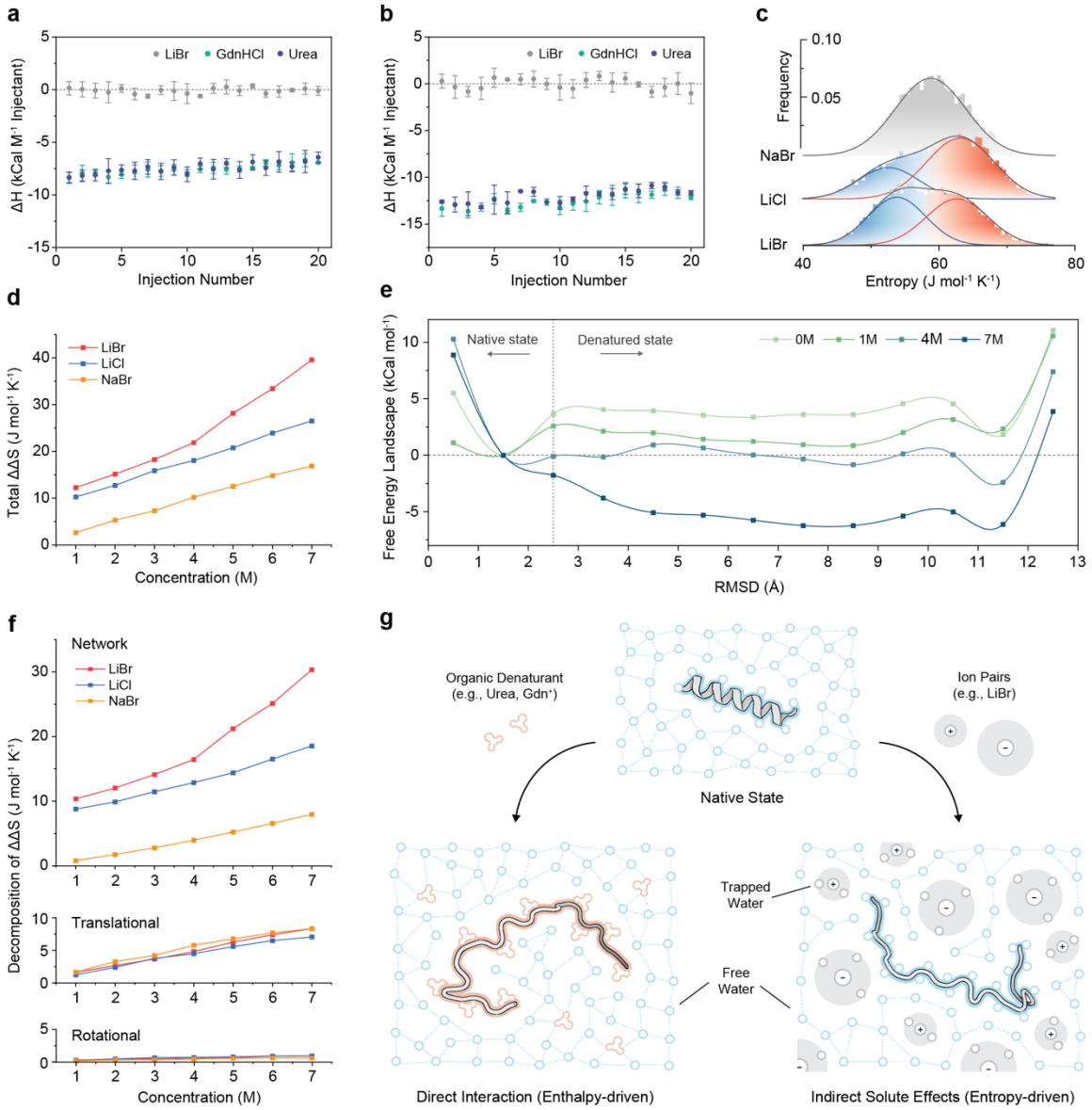

Fig. 2 | Protein conformational changes come from indirect solute effects manifested as water network entropy. a-b, Reaction enthalpy of interactions between proteins (**a,** DHFR, **b,** fibronectin) and denaturants (LiBr, urea, and GdnHCl) as measured by isothermal titration calorimetry. Data are presented as mean ± s.d. (n = 3). **c,** Distributions of molecular entropy of water molecules in 7 M LiBr, LiCl, and NaBr from MD simulations. **d,** Total entropy penalty decrease in different concentrations of LiBr, LiCl, and NaBr solutions. Data are obtained from MD simulations and calculated via the analytical model (Eq. 1). Data are presented as mean ± s.d. (n = 3), however, the error bars are smaller than the data point size. **e,** Free energy landscape of an α-helix peptide (20 amino acids) in pure water and 1, 4, 7 M LiBr from MD simulations. **f,** Decomposition of the total entropy penalty decrease presented in **d**. **g,** Mechanistic comparison of protein unfolding driven by direct interaction and indirect solute effects.

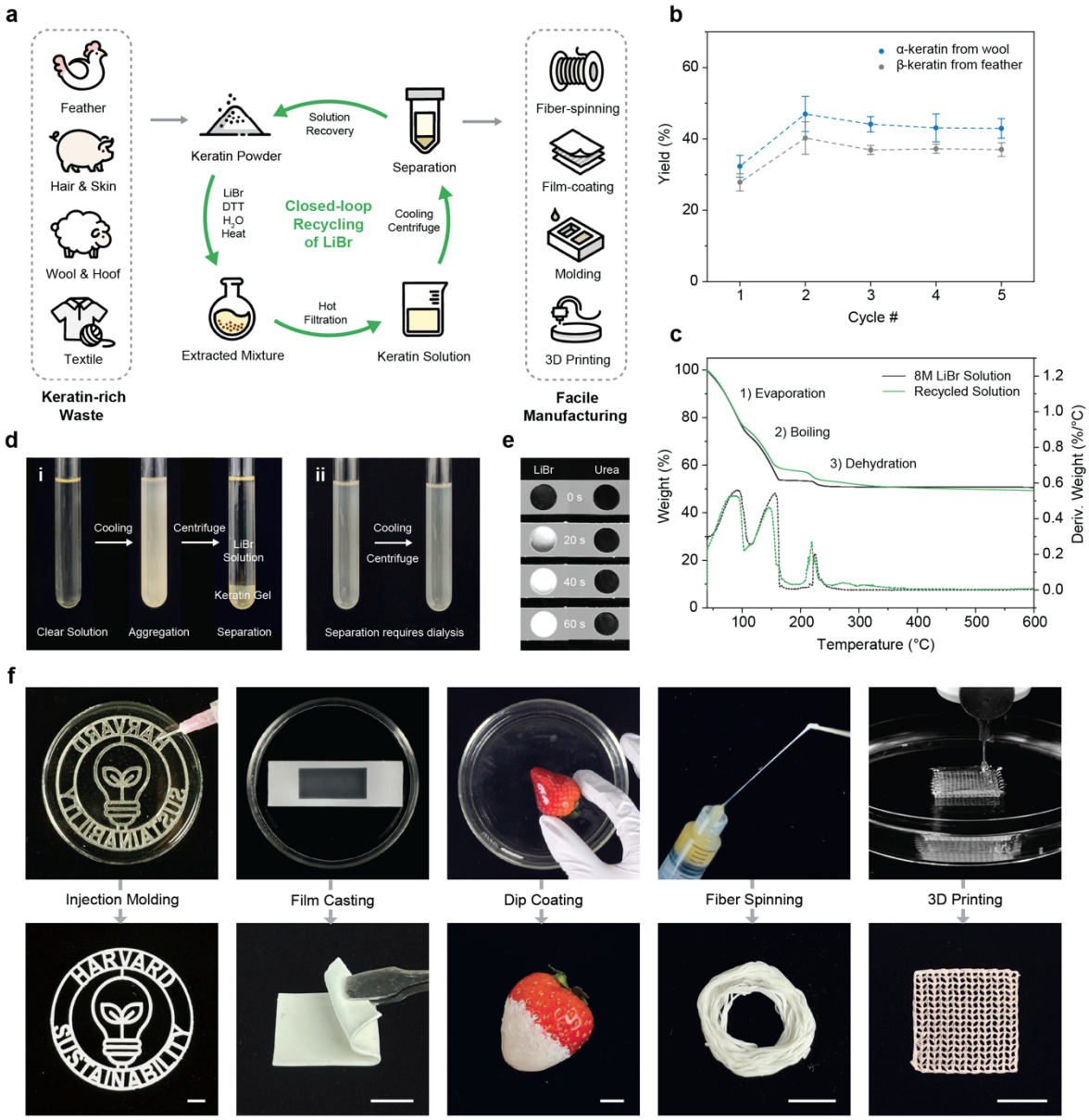

Fig. 3 | Sustainable regeneration of keratin waste with facile manufacturing. a, Schematic showing the regeneration protocol of keratin waste with closed-loop recycling of LiBr solution. **b**, Extraction yield of α-keratin from wool and β-keratin from goose down. Data are presented as mean ± s.d. (n = 7 for α-keratin, n = 3 for β-keratin). **c**, Comparison of the TGA profile shows no major change in the LiBr solution after 5 cycles of extraction. **d**, Keratin solution extracted with LiBr undergoes spontaneous aggregation upon cooling, and can be easily separated into condensed gel after centrifuging (i). Keratin solution extracted with urea remains homogenous after the same process, requiring dialysis for separation (ii). **e**, Immersing extracted keratin on coverslips with transparent well spacers in water. Keratin gel from LiBr extraction quickly turns into a white solid phase, while keratin solution from urea extraction remains soluble. **f**, Facile manufacturing strategies including injection molding, film casting, dip coating, fiber spinning, and 3D printing. Scale bars, 1 cm.

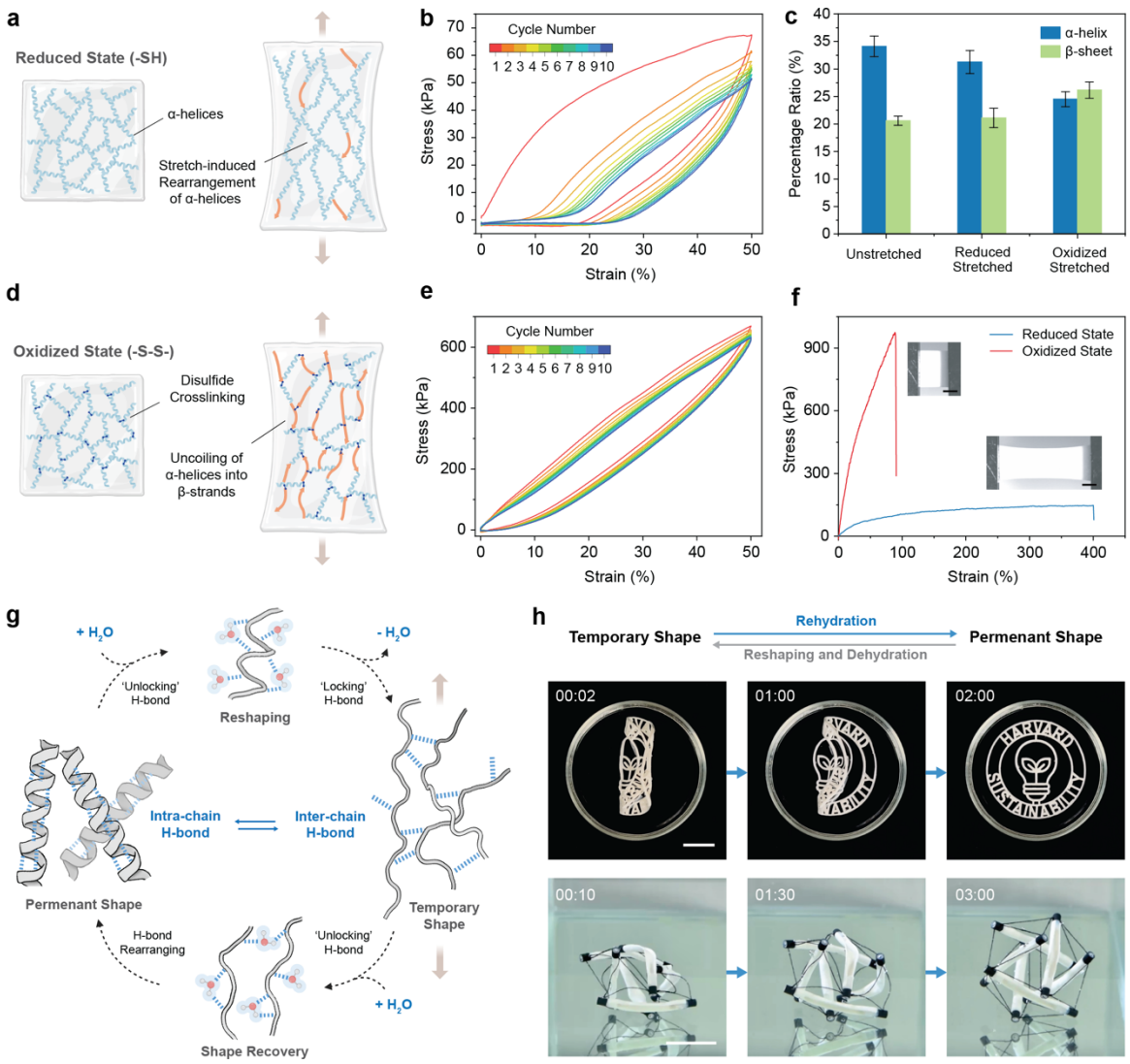

Fig. 4 | Tunable mechanical properties and shape-memory effect of regenerated keratin. a, Schematic of the α-keratin in reduced state and directional rearrangement of α-helices induced by stretching. **b**, Cyclic loading of reduced keratin to 50% strain. **c**, Change of secondary structure percentage under 50% strain quantified from Raman deconvolution of amide I band. A more significant decrease of α-helix can be observed within oxidized sample, indicating the uncoiling of helices into metastable β-sheets (n = 3). **d**, Schematic of the α-keratin in oxidized state and uncoiling of helices upon stretch. **e**, Cyclic loading of oxidized keratin to 50% strain. **f**, Stress-strain curves of reduced and oxidized keratin until fracture. Scale bars, 2 mm. **g**, Schematic of the shape memory effect triggered by hydration signal. **h**, Demonstration of shape memory effect with a badge model and a tensegrity structure. Scale bars: 3 cm.

References

1. Hofmeister, F. Zur Lehre von der Wirkung der Salze. *Archiv f. experiment. Pathol. u. Pharmakol* **24**, 247–260 (1888).
2. Jungwirth, P. & Cremer, P. S. Beyond Hofmeister. *Nature Chem* **6**, 261–263 (2014).
3. Bello, J. & Bello, H. R. Evidence from model peptides relating to the denaturation of proteins by lithium salts. *Nature* **194**, 681–682 (1962).
4. Feughelman, M., Haly, A. R. & Mason, P. Contraction of Keratin Fibres in Aqueous Lithium Bromide. *Nature* **196**, 957–958 (1962).
5. Carpenter, D. C. & Lovelace, F. E. The Influence of Neutral Salts on the Optical Rotation of Gelatin. III. Effect of the Halides of Lithium, Sodium, Rubidium and Cesium1. *J. Am. Chem. Soc.* **57**, 2337–2342 (1935).
6. Mandelkern, L., Halpin, J. C., Diorio, A. F. & Posner, A. S. Dimensional Changes in Fibrous Macromolecules: The System α-Keratin-Lithium Bromide. *J. Amer. Chem. Soc.* **84**, 1383–1391 (1962).
7. Bello, J. & Bello, H. R. Interaction of Model Peptides with Water and Lithium Bromide. *Nature* **190**, 440–441 (1961).
8. Balos, V. *et al.* Time-resolved terahertz–Raman spectroscopy reveals that cations and anions distinctly modify intermolecular interactions of water. *Nat. Chem.* **14**, 1031–1037 (2022).
9. Mazzini, V. & Craig, V. S. J. Volcano Plots Emerge from a Sea of Nonaqueous Solvents: The Law of Matching Water Affinities Extends to All Solvents. *ACS Cent. Sci.* **4**, 1056–1064 (2018).
10. Bellissent-Funel, M.-C. *et al.* Water Determines the Structure and Dynamics of Proteins. *Chem. Rev.* **116**, 7673–7697 (2016).
11. Levy, Y. & Onuchic, J. N. Water mediation in protein folding and molecular recognition. *Annu Rev Biophys Biomol Struct* **35**, 389–415 (2006).
12. Dill, K. A., Truskett, T. M., Vlachy, V. & Hribar-Lee, B. Modeling Water, the Hydrophobic Effect, and Ion Solvation. *Annual Review of Biophysics* **34**, 173–199 (2005).
13. Shakhnovich, E. Protein Folding Thermodynamics and Dynamics: Where Physics, Chemistry, and Biology Meet. *Chem. Rev.* **106**, 1559–1588 (2006).
14. Xie, W. J. & Gao, Y. Q. A Simple Theory for the Hofmeister Series. *J. Phys. Chem. Lett.* **4**, 4247–4252 (2013).
15. Ashworth, C. Plastics from proteins. *Nat Rev Chem* **6**, 165–165 (2022).
16. Rosenboom, J.-G., Langer, R. & Traverso, G. Bioplastics for a circular economy. *Nat Rev Mater* **7**, 117–137 (2022).
17. Senthilkumar, N., Chowdhury, S. & Sanpui, P. Extraction of keratin from keratinous wastes: current status and future directions. *J Mater Cycles Waste Manag* **25**, 1–16 (2023).
18. Niinimäki, K. *et al.* The environmental price of fast fashion. *Nat Rev Earth Environ* **1**, 189–200 (2020).
19. Sun, J. *et al.* Bioinspired Processing of Keratin into Upcycled Fibers through pH-Induced Coacervation. *ACS Sustainable Chem. Eng.* **11**, 1985–1994 (2023).
20. Fang, W., Fan, R., Aranko, A. S., Hummel, M. & Sixta, H. Upcycling of Keratin Wastes in Sustainable Textile Fiber Applications. *ACS Sustainable Chem. Eng.* **11**, 14807–14815 (2023).
21. Zhu, S. *et al.* Using Wool Keratin as a Structural Biomaterial and Natural Mediator to Fabricate Biocompatible and Robust Bioelectronic Platforms. *Adv Sci (Weinh)* **10**, e2207400 (2023).

22. Dalton, C. J. & Lemmon, C. A. Fibronectin: Molecular Structure, Fibrillar Structure and Mechanochemical Signaling. *Cells* **10**, 2443 (2021).
23. Feinberg, A. W. & Parker, K. K. Surface-Initiated Assembly of Protein Nanofabrics. *Nano Lett.* **10**, 2184–2191 (2010).
24. Ahn, S. *et al.* Self-Organizing Large-Scale Extracellular-Matrix Protein Networks. *Advanced Materials* **27**, 2838–2845 (2015).
25. Ahn, S., Lee, K. Y., Parker, K. K. & Shin, K. Formation of Multi-Component Extracellular Matrix Protein Fibers. *Sci Rep* **8**, 1913 (2018).
26. Deravi, L. F. *et al.* Differential Contributions of Conformation Extension and Domain Unfolding to Properties of Fibronectin Nanotextiles. *Nano Lett.* **12**, 5587–5592 (2012).
27. Privalov, P. L. Stability of proteins: small globular proteins. *Adv Protein Chem* **33**, 167–241 (1979).
28. O'Brien, E. P., Dima, R. I., Brooks, B. & Thirumalai, D. Interactions between Hydrophobic and Ionic Solutes in Aqueous Guanidinium Chloride and Urea Solutions: Lessons for Protein Denaturation Mechanism. *J. Am. Chem. Soc.* **129**, 7346–7353 (2007).
29. Stumpe, M. C. & Grubmüller, H. Interaction of Urea with Amino Acids: Implications for Urea-Induced Protein Denaturation. *J. Am. Chem. Soc.* **129**, 16126–16131 (2007).
30. Skipper, N. T. & Neilson, G. W. X-ray and neutron diffraction studies on concentrated aqueous solutions of sodium nitrate and silver nitrate. *J. Phys.: Condens. Matter* **1**, 4141 (1989).
31. Tielrooij, K. J., Garcia-Araez, N., Bonn, M. & Bakker, H. J. Cooperativity in Ion Hydration. *Science* **328**, 1006–1009 (2010).
32. Jorgensen, W. L., Chandrasekhar, J., Madura, J. D., Impey, R. W. & Klein, M. L. Comparison of simple potential functions for simulating liquid water. *The Journal of Chemical Physics* **79**, 926–935 (1983).
33. Lin, S.-T., Maiti, P. K. & Goddard, W. A. I. Two-Phase Thermodynamic Model for Efficient and Accurate Absolute Entropy of Water from Molecular Dynamics Simulations. *J. Phys. Chem. B* **114**, 8191–8198 (2010).
34. Roget, S. A., Heck, T. R., Carter-Fenk, K. A. & Fayer, M. D. Ion/Water Network Structural Dynamics in Highly Concentrated Lithium Chloride and Lithium Bromide Solutions Probed with Ultrafast Infrared Spectroscopy. *J. Phys. Chem. B* **127**, 4532–4543 (2023).
35. Harano, Y. & Kinoshita, M. Translational-Entropy Gain of Solvent upon Protein Folding. *Biophys. J.* **89**, 2701–2710 (2005).
36. Okur, H. I. *et al.* Beyond the Hofmeister Series: Ion-Specific Effects on Proteins and Their Biological Functions. *J. Phys. Chem. B* **121**, 1997–2014 (2017).
37. Fiorin, G., Klein, M. L. & Hénin, J. Using collective variables to drive molecular dynamics simulations. *Molecular Physics* **111**, 3345–3362 (2013).
38. Miserez, A., Wasko, S. S., Carpenter, C. F. & Waite, J. H. Non-entropic and reversible long-range deformation of an encapsulating bioelastomer. *Nat Mater* **8**, 910–916 (2009).
39. Cera, L. *et al.* A bioinspired and hierarchically structured shape-memory material. *Nat Mater* **20**, 242–249 (2021).

421 # Methods

422 **Additional methods**

423 Additional methods, along with additional analyses and discussions, can be found in
424 supplementary materials.

425 ***Escherichia coli* dihydrofolate reductase expression**

426 **Cell culture.** *E. coli* dihydrofolate reductase (DHFR, UniProt: P0ABQ4) (wild-type or W30C
427 mutant) was overexpressed in BL21(DE3) *E. coli* cells. The plasmid was synthesized by GenScript
428 Biotech with pET-28a(+) vector and C-terminus 6xHis-tag. All the cell culture were conducted in
429 Terrific Broth (TB) medium (BD Difco™), supplemented with 0.4% (v/v) glycerol (RPI), 4 g L^{-1}
430 glucose (Sigma-Aldrich), 25 mM MOPS (Sigma-Aldrich, pH=7.2), 0.4 mM citric acid (VWR
431 Chemicals BDH®), 40 µl L^{-1} 1% (w/v) ferric ammonium citrate (AMRESCO) solution, and 50 µg
432 ml^{-1} kanamycin (Millipore-Sigma). All the concentrations denoted here are final concentrations.
433 2% (v/v) frozen cell stock solution of BL21(DE3) *E. coli* cells transformed with DHFR (wild-type
434 or W30C mutant) plasmid was used for a small overnight (~12 h) culture at 37 °C with shaking at
435 250 rpm. 2% (v/v) overnight culture solution was used to start the production culture, initially at
436 37 °C with shaking at 250 rpm. After 3.5 hours at which the cell growth started the mid-log phase
437 with an optical density of around 0.6 at 600 nm, isopropyl β-D-thiogalactopyranoside (IPTG, RPI)
438 was added to a final concentration of 100 µM to induce the protein overexpression. The
439 temperature was decreased to 18 °C, with shaker speed kept as 250 rpm. The cell pellets were
440 harvested after 12-hour low-temperature protein overexpression through centrifugation.

441 **Protein purification.** Three different buffers were used in DHFR protein purification: Lysis buffer
442 [100 mM bicine (Sigma-Aldrich), 5 mM imidazole (Millipore-Sigma OmniPur®), 250 mM NaCl
443 (VWR Chemicals BDH®), pH=9]; Buffer A [20 mM Tris (J.T. Baker™), 5 mM imidazole, 250 mM

444 NaCl, pH=8.5]; Buffer B [20 mM Tris, 50 mM imidazole, 250 mM NaCl, pH=8]. Every 1 g cell
445 pellet (from 50 ml cell culture solution) was resuspended in 1.5 ml lysis buffer, supplemented with
446 0.01% (v/v) Nuclease (Millipore-Sigma Benzonase®), 1% (v/v) Protease Inhibitor Cocktail Set II
447 (Millipore-Sigma Calbiochem®), and 1 mg ml^{-1} lysozyme (Thermo Fisher Scientific). All the
448 concentrations denoted here are final concentrations. The resuspended solution was then sonicated,
449 centrifuged with supernatant collected. cOmplete™ His-Tag Purification Resin (Roche) was used
450 to further isolate DHFR protein from supernatant in gravity flow columns (Bio-Rad). Buffer A
451 was first used to wash away non-bound proteins and other cell debris, followed by elution of Buffer
452 B, where DHFR was washed out and collected. Only the fractions with $A_{280}/A_{260} > 1.7$ were pooled
453 based on the absorbance measurement with a NanoDrop spectrophotometer (Thermo Fisher
454 Scientific). DHFR was then washed into 20 mM Tris buffered saline (pH=7.0, with 250 mM NaCl)
455 and concentrated into a final concentration of 3 mg ml^{-1} using ultrafilter (Sartorius Vivaspin®).
456 Mass spectrometry (Bruker Impact II q-TOF) was used to confirm that DHFR (both wild-type and
457 W30C mutant) was successfully synthesized and purified, after which protein solution was
458 aliquoted and stored in -70 °C.

459 **Turbidity assay**

460 Turbidity measurements at OD_{405} were performed using a Biotek PowerWave HT 340 microplate
461 reader. For each condition, protein solutions was mixed with solutions of LiBr, LiCl, and NaBr
462 (Sigma-Aldrich) to a final concentration of 0.4 mg ml^{-1} for DHFR or 0.1 mg ml^{-1} for human
463 fibronectin (BD Biosciences), with a total volume of 100 µl in a 96-well plate. Samples were then
464 immediately placed into the microplate reader and OD_{405} was continuously measured for 1 h at
465 room temperature. For keratin, 80 mg of cleaned wool (R. H. Lindsay Wool Company) was soaked
466 into 4 ml of salt solutions with 0.1 M DTT (Sigma-Aldrich) in quartz cuvettes, then heated to 70 °C

467 to accelerate the denaturation kinetics. Samples of the solutions were taken at 24 h and 48 h, added
468 into 96-well plate, and cooled at room temperature before OD_{405} measurement. Photos recording
469 the condition of the solution were taken after cooling the cuvette at room temperature for 1h.

470 **FTIR and TG-FTIR**

471 All FTIR measurements were conducted using a Nicolet iS50 FTIR spectrometer. Protein solutions
472 with final concentrations of 1 mg ml^{-1} DHFR, 0.5 mg ml^{-1} fibronectin, and 1 mg ml^{-1} keratin (α-
473 keratin from Angora wool, R. H. Lindsay Wool Company; β-keratin from goose down, Dream
474 Solutions USA), respectively, were prepared with a gradient of LiBr concentrations ranging from
475 0 to 8 M, then stabilized for at least 3 h prior to measurements. During acquisition, background
476 information was initially recorded by applying pure LiBr solutions onto the ATR crystal, which
477 was then replaced by the corresponding protein solutions, with a total of 64 scans collected for
478 each sample. Solid samples, including regenerated keratins and raw materials, were measured
479 using the same ATR-FTIR setup. Gas phase FTIR coupled with TGA was collected using the same
480 equipment connected to the Discovery TGA 550. Data analysis and background subtraction were
481 carried out with OMNIC v.9.2.86 software.

482 **Raman and polarized Raman**

483 Raman experiments were performed with a Horiba LabRam HR Evolution Raman confocal system
484 (633nm excitation, 50x, 0.5NA, 13mW). For DHFR experiment, a customized imaging chamber
485 made by sandwiching a 1 mm thick PDMS (Sylgard™ 184, Dow Corning) well between two glass
486 slides (Supplementary Fig. 4) was loaded with a solution of 3 mg ml^{-1} DHFR and 2 M LiBr. Each
487 spectrum was collected with 600 gr mm^{-1}, 180 s acquisition time and 2 accumulations. For solid
488 samples, 1800 gr mm^{-1}, 60 s acquisition and 4 accumulations were used. For polarized Raman, an

489 additional increment of 6° per step were applied with the highest intensity tracked around 1650
490 cm^{-1}. Data collection and analysis were carried out with Labspec v.6.5.1 software.

491 **Dynamic light scattering**

492 DLS experiments were performed using a Malvern Zeitasizer Pro system. Fibronectin in LiBr
493 solutions were prepared with a final concentration of 0.5 mg ml^{-1}, stabilized for at least 3 h, and
494 filtered through a 0.22 µm PTFE filter (VWR) before transferred into 40 µl cuvettes (Malvern
495 Panalytical) for measurement. Keratin solutions after extraction were diluted to approximately 1
496 mg ml^{-1}, filtered, then transferred into 1 ml cuvettes (Malvern Panalytical). Samples were heated
497 to 70 °C for 30 min, then stabilized at designated temperature for 10 min before measurement. A
498 reversible transition between smaller diameters at high temperature and larger diameters at low
499 temperature can be observed within individual samples. Data collection and analysis were carried
500 out with ZS Xplorer v.3.0.0.53 software.

501 **Scanning electron microscopy**

502 Samples were mounted on a 12.5 mm diameter SEM stub covered with carbon tape, then sputtered-
503 coated with Pt/Pd with an EMS 150T ES sputter coater with 10 nm thickness. SEM images were
504 taken with a Zeiss Gemini 360 field emission scanning electron microscope with an electric high
505 tension of 3 kV and SE2 detector.

506 **Isothermal titration calorimetry**

507 ITC experiments were conducted using a Malvern Panalytical MicroCal VP-ITC. During the
508 experiments, the sample chamber was filled with 1.8 ml of 1 mg ml^{-1} DHFR (W30C mutant)
509 solution or 0.5 mg ml^{-1} fibronectin solution, while the syringe was loaded with 100 µM solution
510 of LiBr, urea, or GdnHCl (Sigma-Aldrich). Corresponding control experiments were performed
511 by titrating milli-Q water into the same concentration of protein solution to measure and subtract

512 the dilution heat of proteins. Additionally, parallel control groups were also performed by titrating
513 100 μM ligands into a chamber filled with milli-Q water to measure the dilution heat of ligands,
514 which were found to be significantly smaller than the detectable binding enthalpy between proteins
515 and ligands (Supplementary Fig. 6). Each individual run comprised titrating 7 μl ligand solution
516 25 times into the chamber, with a duration of 12 s, and interval of 240 s, a filter period of 2 s, a stir
517 speed of 309, and temperature controlled at 30 °C. Data collection and analysis including baseline
518 adjustment and integration of enthalpy were carried out with VPViewer2000 v.1.29.1 software.

519 **Molecular dynamics simulations**

520 **General simulation setup**. All the molecular dynamics simulations were conducted with NAMD
521 2.14[40] and analyzed and visualized with VMD 1.9.3[41], unless otherwise denoted. Amber ff14SB
522 force field[42] were used for atomistic protein simulation, combined with TIP3P water model[43] for
523 explicit solvation and Li/Merz ion parameters[44] for monovalent ions. All initial configurations of
524 simulation box were prepared using tLEaP program[45], followed by minimization, heating, constant
525 pressure (NPT) equilibration, and constant volume (NVT) equilibration. All the production
526 simulations were run under constant particle number, constant volume, and constant temperature
527 (i.e., canonical ensemble (NVT)). Periodic boundary condition was applied to prevent the
528 boundary effect. Langevin thermostat with damping coefficient of 1 ps^{-1} was used to control
529 simulation temperature as 298 K, without coupling hydrogen atoms. Electrostatic and van der
530 Waals interactions were cut off beyond 12 Å. Particle Mesh Ewald (PME) method was employed
531 to deal with long-range electrostatic interactions. Rigid bond constraints between hydrogen and
532 any other atoms were applied through SHAKE/RATTLE algorithm. The integration time step was
533 set as 2 fs with short-range nonbonded forces updated every 2 fs and long-range electrostatic forces
534 updated every 4fs.

Initial configuration preparation and equilibration. To ensure that total number of ions and water molecules are correctly determined for all salts and concentrations, we first decided the simulation box sizes and thus ion numbers. All the simulation boxes were fixed to the size with three dimensions around 50 Å. Water molecules were initially placed using tLEaP program[45], the numbers of which were then adjusted according to volume changes after 100 ps minimization, 200 ps heating, and 2 ns constant pressure (NPT) equilibration. After the water molecule number corrections, another round of 100 ps minimization, 200 ps heating, 2 ns constant pressure (NPT) equilibration, plus 2 ns constant volume (NVT) equilibration, were conducted to ensure the correct setup and complete equilibration of simulation systems.

Water structure characterization. The equilibrated initial configurations containing water molecules and ions were prepared as stated above. The production simulations for water structure characterization were run for 100 ns with trajectories recorded every 10 ps. The radial distribution function *g(r)* between cations (or anions) and oxygen atoms of water can be used to characterize local water structure around ions. It was calculated via VMD and averaged among all cations (or anions) and all trajectory frames with the definition as

$$g(r) = \frac{dn_r}{4\pi r^2 \cdot dr \cdot \rho_{\text{bulk}}} \tag{2}$$

where dn_r is the number of oxygen atoms of water within the shell of thickness at the distance r, $4\pi r^2 \cdot dr$ is the volume of the shell, ρ_{bulk} is the bulk average density of oxygen atoms of water in the simulation box.

Water entropy calculation. The equilibrated initial configurations containing water molecules and ions were prepared as stated above. The production simulations for water entropy calculation were run for 20 ps[33] with trajectories recorded every 2 fs. All the water entropy calculations were

557 conducted based on Two-Phase Thermodynamic (2PT) model[33,46] using corresponding open
558 source program[47].

559 The resulting histograms were fit with two Gaussian distributions with no boundary
560 conditions. Initial values of peak centers were determined using local minimums of 2nd derivative.
561 For LiBr and LiCl, fitting achieved convergence with Chi-Square tolerance value of 10^{-6}. For NaBr,
562 one peak will collapse to zero and only a single peak remained upon convergence.

563 **Protein free energy landscape construction.** To examine changes in free energy that drives
564 denaturation, we used metadynamics simulation to explore the free energy landscape of the
565 complex molecular system including water, ions, and protein. A short alanine-based peptide with
566 20 amino acids (AAAAKAAAAKAAAAKAAAAK), which has been confirmed experimentally[48]
567 to be a stable alpha helix structure in pure water, was adopted as the model protein to study the
568 difference of protein free energy landscapes under different concentrations of LiBr. We used
569 ColabFold v1.5.5[49] to obtain the initial atomistic protein structure, with N-terminus acetylated and
570 C-terminus amidated using PyMOL 2.5.5. The equilibrated initial configurations containing
571 protein, water molecules and ions were prepared as stated above. Well-tempered metadynamics
572 simulations were implemented for protein free energy landscape construction using Colvars
573 module[37] on top of standard molecular dynamics simulations as stated above. Root mean square
574 displacement (RMSD) from the backbone of native alpha helix protein structure was selected as
575 the collective variable to guide the sampling of unfolded confirmations. After the first run of
576 metadynamics simulation, two more protein confirmations (Supplementary Fig. 7a) with medium
577 RMSD (6 Å) and large RMSD (12 Å) respectively, were chosen as two other start structures. In
578 total, nine metadynamics simulations for each LiBr concentration, started from three different
579 initial protein conformations, were conducted. Each simulation was run for around 2 μs with

trajectory recorded every 100 ps (Supplementary Fig. 7b,c). Convergence of metadynamics simulations was examined using block analysis via the open-source, community-developed PLUMED library, version 2.8.3[50]. Six converged simulations out of nine for each LiBr concentration were used for final protein free energy landscape construction (Supplementary Fig. 8-11).

Analytical model of entropy penalty decrease

The protein unfolding reaction is defined as

$$F \leftrightarrows U \tag{3}$$

where F is the folded state and U is the unfolded state. For folded proteins, since they can maintain stable structures in pure water solution (or very low concentration NaCl solution), the free energy change ΔG_{water} of the unfolding reaction in pure water should be positive, i.e.,

$$\Delta G_{\text{water}} > 0 \tag{4}$$

According to the unfolding experiments presented in this work, LiBr has the strongest capability of unfolding (denaturing) proteins, followed by LiCl. NaBr cannot denature those tested proteins in this work. Therefore, the free energy changes of the unfolding reaction in different solution environments can be ranked as follow,

$$\Delta G_{\text{LiBr}} < \Delta G_{\text{LiCl}} < \Delta G_{\text{NaBr}} < \Delta G_{\text{water}} \tag{5}$$

where ΔG_{LiBr} and ΔG_{LiCl} for some proteins in high concentration salt solutions are negative (i.e., the unfolding reaction is favored).

The difference between free energy changes of the unfolding reaction in salt solutions ΔG_{salt} and that in pure water ΔG_{water} can be written as

$$\begin{aligned} \Delta\Delta G &= \Delta G_{\text{salt}} - \Delta G_{\text{water}} < 0 \\ &= \Delta H_{\text{salt}} - \Delta H_{\text{water}} - T\Delta S_{\text{salt}} - (-T\Delta S_{\text{water}}) \\ &= \Delta\Delta H - T\Delta\Delta S \end{aligned} \tag{6}$$

where enthalpy change difference $\Delta\Delta H$ equals to 0 given the ITC data (Fig. 2a-b) that no direct interaction between proteins and ions was observed. Thus, we have

$$\Delta\Delta G = -T\Delta\Delta S < 0 \tag{7}$$

where $\Delta\Delta S$ is the entropy penalty decrease due to high concentration salts and should be positive.

Entropy penalty decrease caused by high concentration salts can be written as

$$\begin{aligned}\Delta\Delta S &= \Delta S_{\text{salt}} - \Delta S_{\text{water}} > 0 \\ &= \Delta S_{\text{salt}}^{\text{protein}} + \Delta S_{\text{salt}}^{\text{solution}} - \left(\Delta S_{\text{water}}^{\text{protein}} + \Delta S_{\text{water}}^{\text{solution}}\right) \\ &= \Delta S_{\text{salt}}^{\text{solution}} - \Delta S_{\text{water}}^{\text{solution}}\end{aligned} \tag{8}$$

where protein conformational entropy changes $\Delta S^{\text{protein}}$ during unfolding is independent of solutions and thus cancel with each other, $\Delta S^{\text{solution}}$ is the solution entropy change.

The solution entropy S^{solution} is composed of two parts, i.e., molecular entropy and network entropy. Molecular entropy is composed of translational, rotational, and vibrational entropy of water molecules themselves. Network entropy comes from the collective behavior of water network, which considers different combinations water molecules can have to form a network. Therefore, the solution entropy change during protein unfolding can be expressed as

$$\Delta S^{\text{solution}} = \Delta S^{\text{translation}} + \Delta S^{\text{rotation}} + \Delta S^{\text{vibration}} + \Delta S^{\text{network}} \tag{9}$$

Consider a water network with N water molecules (so-called *free* water molecules since they are not bound by either proteins or ions), the number of microstates for each water molecule inside the network can be expressed as

$$\Omega = \left(N^{\text{free}} - 1\right)\left(N^{\text{free}} - 2\right)\left(N^{\text{free}} - 3\right)\left(N^{\text{free}} - 4\right) \tag{10}$$

given one water molecule can form four hydrogen bonds with other water molecules in the network.

Then the network entropy of each water molecule is

$$S^{\text{network}} = k_{\text{B}} \ln(\Omega) = k_{\text{B}} \ln\left(\left(N^{\text{free}} - 1\right)\left(N^{\text{free}} - 2\right)\left(N^{\text{free}} - 3\right)\left(N^{\text{free}} - 4\right)\right) \tag{11}$$

where

$$\Delta S^{\text{network}} = -k_{\text{B}} \ln\left(\left(N^{\text{free}} - 1\right)\left(N^{\text{free}} - 2\right)\left(N^{\text{free}} - 3\right)\left(N^{\text{free}} - 4\right)\right) \tag{12}$$

The entropy penalty decrease originated from the shrinkage of intact water network size in high salt concentration systems can be expressed as

$$\begin{aligned}
\Delta\Delta S^{\text{network}} &= \Delta S_{\text{salt}}^{\text{network}} - \Delta S_{\text{water}}^{\text{network}} \\
&= -k_{\text{B}} \ln\left(\frac{\left(N_{\text{salt}}^{\text{free}} - 1\right)\left(N_{\text{salt}}^{\text{free}} - 2\right)\left(N_{\text{salt}}^{\text{free}} - 3\right)\left(N_{\text{salt}}^{\text{free}} - 4\right)}{\left(N_{\text{water}}^{\text{total}} - 1\right)\left(N_{\text{water}}^{\text{total}} - 2\right)\left(N_{\text{water}}^{\text{total}} - 3\right)\left(N_{\text{water}}^{\text{total}} - 4\right)}\right) \\
&\doteq -4k_{\text{B}} \ln\left(\frac{N_{\text{salt}}^{\text{free}}}{N_{\text{water}}^{\text{total}}}\right) \\
&= -4k_{\text{B}} \ln \phi
\end{aligned} \tag{13}$$

where $N_{\text{water}}^{\text{total}}$ is the total number of water molecules in pure water systems as all water molecules here are considered as *free* , both $N_{\text{salt}}^{\text{free}}$ and $N_{\text{water}}^{\text{total}}$ are normally much larger than 1 (i.e., $\gg 1$), $\phi = \frac{N_{\text{salt}}^{\text{free}}}{N_{\text{water}}^{\text{total}}}$ is the ratio of free water number in salt solution to that of pure water system.

Finally, we have

$$\begin{aligned}
\Delta\Delta S &= \Delta S_{\text{salt}}^{\text{solution}} - \Delta S_{\text{water}}^{\text{solution}} \\
&= \Delta\Delta S^{\text{translation}} + \Delta\Delta S^{\text{rotation}} + \Delta\Delta S^{\text{vibration}} + \Delta S^{\text{network}} \\
&= \Delta\Delta S^{\text{translation}} + \Delta\Delta S^{\text{rotation}} + \Delta\Delta S^{\text{vibration}} - 4k_{\text{B}} \ln \phi
\end{aligned} \tag{14}$$

where $\Delta\Delta S^{\text{translation}}$, $\Delta\Delta S^{\text{rotation}}$, and $\Delta\Delta S^{\text{vibration}}$ can be expressed as follows,

$$\begin{aligned}
\Delta\Delta S^{\text{j}} &= \Delta S_{\text{salt}}^{\text{j}} - \Delta S_{\text{water}}^{\text{j}} \\
&= \left(S_{\text{salt}}^{\text{j-bound}} - S_{\text{salt}}^{\text{j-free}}\right) - \left(S_{\text{water}}^{\text{j-bound}} - S_{\text{water}}^{\text{j-free}}\right) \\
&= S_{\text{water}}^{\text{j-free}} - S_{\text{salt}}^{\text{j-free}}
\end{aligned} \tag{15}$$

where j denotes translational or rotational or vibrational components of solution entropy, the S^{j} of bound water molecules by proteins are assumed to be independent of their solution environments and thus cancel out each other. All the parameters in above equation ($\Delta\Delta S^{\text{translation}}$, $\Delta\Delta S^{\text{rotation}}$, $\Delta\Delta S^{\text{vibration}}$, and ϕ) can be obtained through molecular dynamics simulation and Two-Phase Thermodynamic (2PT) calculation[33,46].

640 **Keratin extraction protocol**

641 The pretreatment of keratin-rich sources (Angora wool, Merino wool shirt, and goose down from
642 the R. H. Lindsay Wool Company, Merino Tech, and Dream Solutions USA, respectively)
643 involves washing with ethanol (VWR 200 proof) in a Soxhlet extractor for 48 h to remove organic
644 residues, followed by rinsing with water and allowing the material to dry at room temperature
645 overnight. Subsequently, long wool fibers were cut into smaller fragments (less than 1 cm in length)
646 to facilitate dispersion in solution. During the extraction process, 10 g of keratin fragments were
647 suspended in a 150 ml aqueous solution containing 8 M LiBr and 0.1 M DTT. The suspension was
648 stirred for 36 h in an insulated environment at 90°C. Afterwards, insoluble residues were filtered
649 through cotton cloth with 80/180 μm mesh size while still hot, then stored at 4°C overnight. A
650 viscous, gel phase of aggregated keratin was observed, and centrifugation (3,000 r.p.m., 4°C)
651 further separated the mixture into an upper phase of LiBr solution and a lower phase of keratin gel.
652 The LiBr solution could then be easily collected and reused in the following extraction cycle along
653 with a new batch of keratin source and DTT. A small amount of 8 M LiBr stock solution were
654 added to compensate the solution loss from filtration process in order to maintain the total volume
655 at 150 ml.

656 The keratin content of the aggregated gel was measured by taking 1 ml of gel and allowing
657 it to fully solidify in water, freeze-dried, then lyophilized to obtain a dehydrated solid and measure
658 its weight. It was found that 1 ml of keratin gel contains 392.8 ± 18.6 mg of α-keratin or 347.9 ±
659 23.7 mg of β-keratin (n = 6). To calculate the extraction yield, the volume of the keratin gel
660 obtained from each batch was measured, multiplied by the corresponding content, and divided by
661 the initial weight of keratin fragments. The denatured keratin gel could be stably stored at 4°C in
662 the absence of oxygen, with a shelf life longer than 6 months.

663 **Thermogravimetric analysis**

664 TGA of the LiBr solution prior to the 1st cycle and the recycled LiBr solution after the 5th cycle
665 were conducted with a Discovery TGA 550. Around 30 mg of solution was loaded onto a platinum
666 HT sample pan, stabilized under nitrogen flow for 10 min before measurement. Experiments were
667 performed by heating samples to 100 °C at a rate of 5 °C min^{-1}, then to 600 °C at a rate of 10 °C
668 min^{-1} in an air flow of 90 ml min^{-1}. The mass of the sample was continuously measured while the
669 evolving gas from the sample was analyzed simultaneously by TG-FTIR. Data collection and
670 analysis were carried out with TRIOS v.5.2.2 software.

671 **Sample preparation**

672 All samples were regenerated using α-keratin gel unless otherwise noted. The reverse mold for
673 injection molding was created by casting PDMS (Sylgard™ 184, Dow Corning) around a 3D
674 printed logo. Keratin gel was injected into the mold and transferred into a water bath until solidified.
675 Film casting and dip coating followed a similar process by casting a layer of gel on glass coverslip
676 or coating targets, then transferred into a water bath. Fiber spinning was achieved by injecting the
677 gel through a 21 gauge needle (BD PrecisionGlide™) at a constant rate of 0.1 ml min^{-1} into a bath
678 of 0.4 M NaH_2PO_4 (Sigma-Aldrich) solution to accelerate the phase transition process. 3D printing
679 was carried out using a Cellink BIO X 3D printer. The keratin gel was extruded into a supporting
680 bath of 25% w/v Pluronic F127 (BASF) under an absolute pressure of 50 kPa and through a 22
681 gauge needle (Nordson EFD Precision Tips) that was moving at a speed of 4 mm s^{-1}. The Pluronic
682 bath was then removed by cooling and rinsing with water.

683 Keratin samples for mechanical tests, Raman and polarized Raman spectra were prepared
684 by film casting a layer of keratin gel onto glass coverslips with a thickness around 0.4 mm, then
685 transferred into a water bath to solidify the gel. Oxidized samples were fabricated by further

transferring into a solution of 1% H_2O_2 for 1 h to reconnect the disulfide bonds. Finally, samples were sectioned into 5 × 20 mm rectangles and stored in water prior to measurements.

The tensegrity structure for the shape memory demonstration was created by oxidizing keratin films in a curled permanent state to form columns as compression units. These units were then interconnected with nylon threads (Singer®) to serve as tension units. Samples were fixed in a distorted temporary state by desiccating for 90 min with addition of external stress.

Mechanical tests

Mechanical tests were performed with a CellScale biaxial tester with 2.5 N load cells. For cyclic stretching curves, samples were tested at a strain rate of 5% per second to a maximum of 50% for 10 cycles. For yield strain measurements, samples were tested at a strain rate of 5% until fracture. Sample thickness was measured with a Mitutoyo Absolute Digimatic digital caliper. The modulus of reduced and oxidized samples was calculated within the 0-50% strain region.

Data availability

All the source data can be readily accessed via https://osf.io/kwmqg/?view_only=62f20b64abb24c4c9ca6e0518f99eecb

Code availability

All the customized codes used for data analysis are available at https://github.com/junlang-liu/Entropy_code.

Methods Section References

40. Phillips, J. C. *et al.* Scalable molecular dynamics on CPU and GPU architectures with NAMD. *J Chem Phys* **153**, 044130 (2020).
41. Humphrey, W., Dalke, A. & Schulten, K. VMD: Visual molecular dynamics. *Journal of Molecular Graphics* **14**, 33–38 (1996).
42. Maier, J. A. *et al.* ff14SB: Improving the Accuracy of Protein Side Chain and Backbone Parameters from ff99SB. *J. Chem. Theory Comput.* **11**, 3696–3713 (2015).
43. Price, D. J. & Brooks, C. L. A modified TIP3P water potential for simulation with Ewald summation. *J Chem Phys* **121**, 10096–10103 (2004).
44. Li, P., Song, L. F. & Merz, K. M. Jr. Parameterization of Highly Charged Metal Ions Using the 12-6-4 LJ-Type Nonbonded Model in Explicit Water. *J. Phys. Chem. B* **119**, 883–895 (2015).
45. Case, D. A. *et al.* The Amber biomolecular simulation programs. *Journal of Computational Chemistry* **26**, 1668–1688 (2005).
46. Lin, S.-T., Blanco, M. & Goddard, W. A., III. The two-phase model for calculating thermodynamic properties of liquids from molecular dynamics: Validation for the phase diagram of Lennard-Jones fluids. *The Journal of Chemical Physics* **119**, 11792–11805 (2003).
47. https://github.com/atlas-nano/2PT.
48. Marqusee, S., Robbins, V. H. & Baldwin, R. L. Unusually stable helix formation in short alanine-based peptides. *Proc Natl Acad Sci U S A* **86**, 5286–5290 (1989).
49. Mirdita, M. *et al.* ColabFold: making protein folding accessible to all. *Nat Methods* **19**, 679–682 (2022).
50. Tribello, G. A., Bonomi, M., Branduardi, D., Camilloni, C. & Bussi, G. PLUMED 2: New feathers for an old bird. *Computer Physics Communications* **185**, 604–613 (2014).

Acknowledgements We thank M. Rosnach for photography and illustrations, S. Mondal for suggestions on molecular simulations, K. Park, E. Serebryany and A. Bitran for discussions on water structure and protein denaturation mechanisms, H. Chang and J. F. Zimmerman for discussions on material properties. K. Shani and Y. Jang for discussions on biological properties and tissue engineering potential of keratin. This work was sponsored by National Institutes of Health (R35GM139571 and R01EY030444 to E.I.S), the John A. Paulson School of Engineering and Applied Sciences at Harvard University (K.K.P.), the National Science Foundation through the Harvard University Materials Research Science and Engineering Center (DMR-2011754 to K.K.P.), the Health@InnoHK program of the Innovation and Technology Commission of the Hong Kong SAR Government, and the Medical & Health Informatics Laboratories at NTT Research, Inc. This work was performed in part at the Harvard University Center for Nanoscale Systems (CNS), a member of the National Nanotechnology Coordinated Infrastructure Network (NNCI), which is supported by the National Science Foundation under NSF award no. ECCS-2025158. The content is solely the responsibility of the authors and does not necessarily represent the official views of NTT Research, Inc.

Author contributions Y.W., J.L., K.K.P., and E.I.S. designed and developed the project. Y.W. and J.L. performed turbidity measurements, tryptophan fluorescence, and FTIR. Y.W., J.L., and D.W. performed ITC experiments. Y.W., J.L., and S.C. performed Raman experiments. J.L. did *E. coli* cell culture, DHFR protein purification and quality control. J.L. conceived the entropy-driven model and developed the analytical model. J.L. conducted all the simulations and related data analysis. Y.W. performed TG-FTIR, polarized Raman, DLS, and TGA measurements. Y.W. performed keratin extraction, demonstrations, and mechanical tests. Y.W. and M.M.P. fabricated keratin fibers and performed SEM imaging. Y.W. and R.I. did SDS-PAGE. Y.W. and J.L. prepared the initial manuscript. Y.W., J.L., K.K.P., and E.I.S. revised the manuscript, with contributions from all the other authors. K.K.P. and E.I.S. supervised the research.

Competing interests A US patent application on the methods for extraction and regeneration of protein wastes has been filed by Harvard University (assignors: Y.W., J.L., K.K.P., and E.I.S.).

Additional information

Supplementary information Supplementary Information is available for this paper.

Correspondence and requests for materials should be addressed to Eugene I. Shakhnovich or Kevin Kit Parker

Peer review information

Reprints and permissions information

Extended Figures

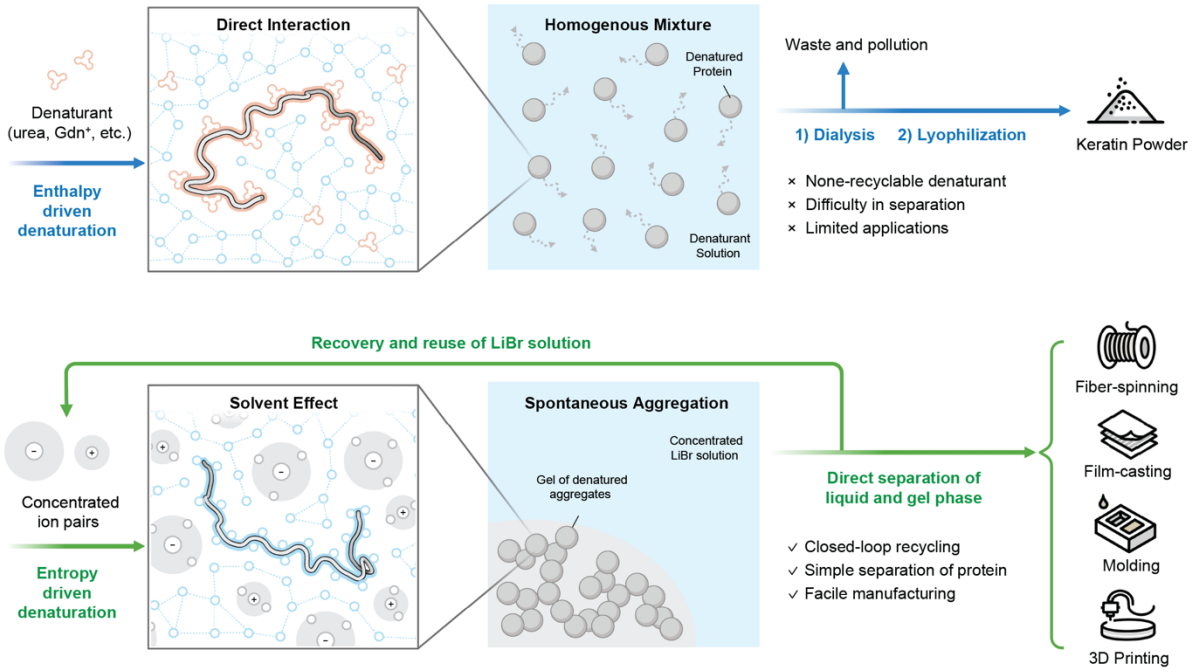

Extended Data Fig. 1 | Sustainable regeneration of protein waste empowered by entropy-driven protein denaturation. Upper, Traditional denaturation methods using urea or guanidine hydrochloride involve direct protein-denaturant interactions, which not only lead to difficulties in protein separation and further applications but also result in plenty of waste and pollution. **Lower,** Due to the absence of direct protein-denaturant interactions, entropy-driven protein denaturation via LiBr enables the sustainable regeneration of protein waste, featured by closed-loop LiBr recycling, simple protein separation, and facile further manufacturing.

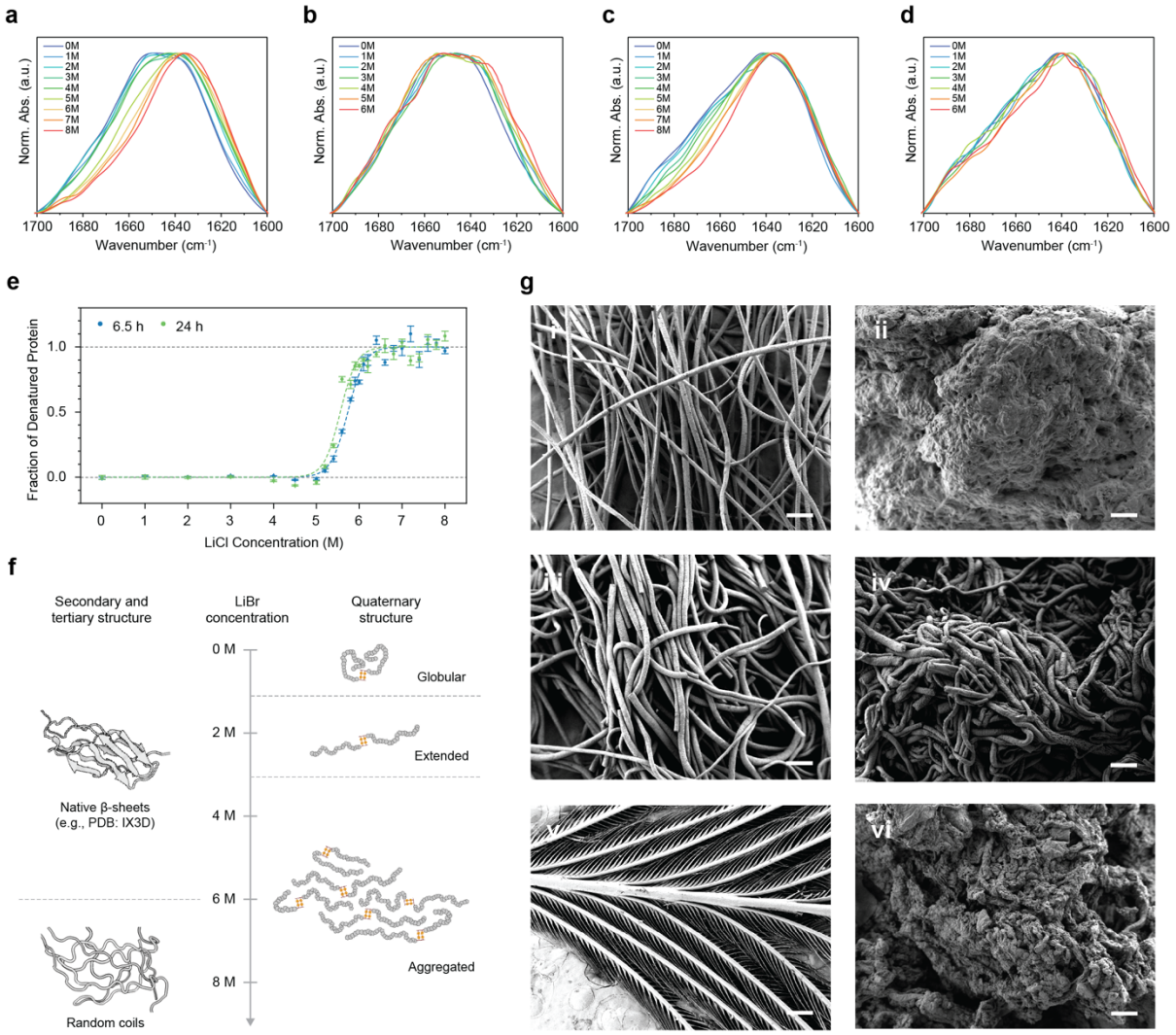

Extended Data Fig. 2 | LiBr, LiCl, and NaBr exhibit different levels of protein conformational change and denaturation capability. a-b, FTIR of the amide I band of DHFR in different concentrations of LiCl (a) and NaBr (b). **c-d**, FTIR of the amide I band of fibronectin in different concentrations of LiCl (c) and NaBr (d). **e,** DHFR unfolding curve in LiCl solution measured by tryptophan fluorescence (dots) and fitted by two-state model (dash lines). Data are presented as mean ± s.d. (n = 3). **f,** Schematics of fibronectin conformational changes under different LiBr concentrations as cross-referenced from FTIR and DLS experiments. Fibronectin conformations start from globular state (0 M), to extended state (~2 M), to aggregation of extended state (4 M-6 M) until aggregation of denatured state (>6 M). **g**, SEM image of wool prior (i) and after 48-hour denaturation with 8 M LiBr (ii), 8 M LiCl (iii), and 7 M NaBr (iv). SEM image of feather prior to (v) and after (vi) 48-hour denaturation with 8 M LiBr. Scale bars, 50 µm.

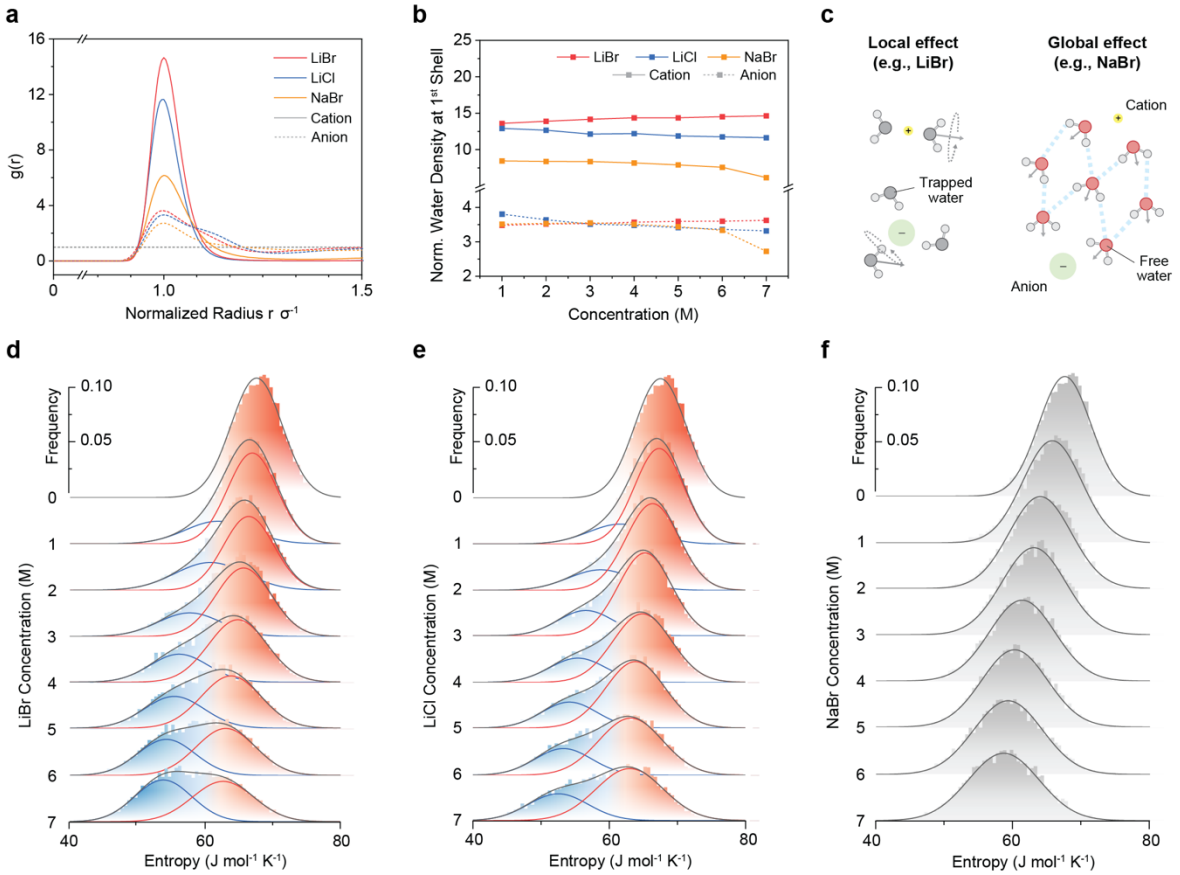

Extended Data Fig. 3 | Local and global effects of ions on water dynamics. a, Radial distribution function *g(r)* of oxygen atoms of water molecules around respective cations (solid) and anions (dashed) in 7 M LiBr, LiCl, and NaBr solution. **b,** Water density at first hydration shell around respective cations (solid) and anions (dashed) in different concentrations of LiBr, LiCl, and NaBr. **c,** Schematics of different ion effects on water dynamics. For LiBr and LiCl, high charge density of Li^+ ion results in localized (bound) water molecules and disrupted water network (left), while NaBr changes water dynamics in a more global manner without breakingK water networks (right). **d-f,** Water molecular entropy distribution in LiBr, LiCl, and NaBr, respectively, at different concentrations.

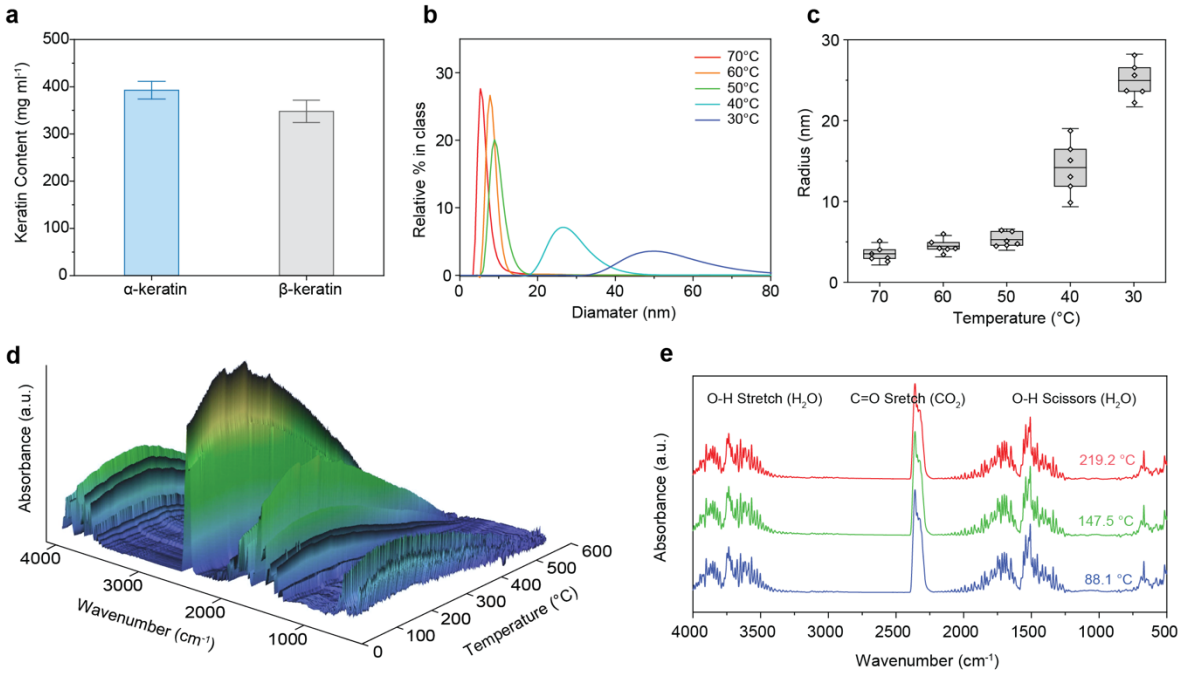

Extended Data Fig. 4 | Properties of keratin during regeneration process and TG-FTIR of recycled LiBr solution. a, Keratin content of aggregated gel after separation. Data are presented as mean ± s.d. (n = 6). **b-c,** Size distribution of denatured keratin in 8 M LiBr solution suggests a spontaneous aggregation as temperature decrease from DLS. **d-e**, TG-FTIR of the LiBr solution recycled after keratin separation.

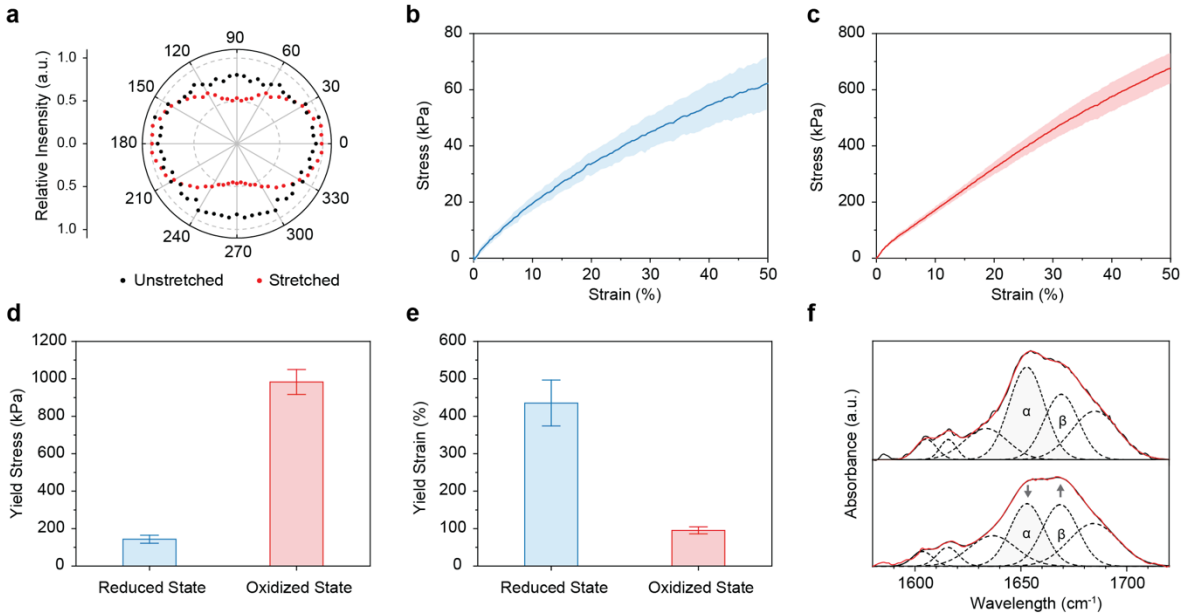

Extended Data Fig. 5 | Mechanical properties and structural behavior of regenerated keratin under stress. a, Polarized Raman of reduced keratin sample. The anisotropy of keratin under 50% strain suggests stretch-induced rearrangement of helices. **b-c,** Stress-strain curve of regenerated keratin in reduced state (b) and oxidated state (c). Data are presented as mean ± s.d. (n = 4). **d-e**, Fracture strain and fracture stress of regenerated keratin in reduced state and oxidized state. Data are presented as mean ± s.d. (n = 6). **f,** Raman spectra of the amide I band of reduced and oxidized keratin under 50% strain. A more significant change of secondary structures within an oxidized sample indicates the uncoiling of helices.